Hindawi
Journal of Nanomaterials
Volume 2022, Article ID 1108865, 16 pages
https://doi.org/10.1155/2022/1108865

Research Article

Theranostic Effect of Folic Acid Functionalized MIL-100(Fe) for Delivery of Prodigiosin and Simultaneous Tracking-Combating Breast Cancer

Fatemeh Mokhtarian,[1] **Banafsheh Rastegari**,[2] **Sedigheh Zeinali**,[1] **Maryam Tohidi**,[1] **and Hamid Reza Karbalaei-Heidari**[3]

[1]*Nanochemical Engineering Department, Faculty of Advanced Technologies, Shiraz University, Shiraz, Iran*
[2]*Diagnostic Laboratory Sciences and Technology Research Center, School of Paramedical Sciences, Shiraz University of Medical Science, Shiraz, Iran*
[3]*Molecular Biology Laboratory, Department of Biology, Faculty of Science, Shiraz University, Shiraz, Iran*

Correspondence should be addressed to Banafsheh Rastegari; brastegari@sums.ac.ir

Received 4 May 2021; Revised 4 November 2021; Accepted 10 December 2021; Published 12 January 2022

Academic Editor: David Cornu

The metal organic framework (MOF) member, MIL-100(Fe), is considered as attractive drug nanocarrier that may be due to the great porosity, colloidal stability, and biocompatibility. In the present study, the new electrochemical synthesis procedure was presented for MIL-100(Fe) building block, and secondly, folic acid (FA) was introduced to the structure for assessing its potential targeted ability to be entrapped by folic acid-positive breast cancer cells, MCF-7. Several techniques such as SEM, XRD, and FT-IR were used to characterize synthesized nanostructures. Both MIL-100(Fe) and MIL-100(Fe)/FA nanoparticles were between 50 to 200 nm with a slightly positive net charge with an area of 1350 and 831.84 m2/g, respectively. The prodigiosin (PG) is selected as a model drug for MIL-100(Fe) and MIL-100(Fe)/FA-targeted delivery owing to its natural fluorescence and cancer cell selectiveness. The loading capacity of both nanocarrier was around 40% with 93-97% loading efficacy. Moreover, the pH-sensitive prodigiosin release rate of MIL-100(Fe)@PG and MIL-100(Fe)/FA@PG showed that 69 to 73% of the drug was released after 24 hours in an acidic environment with around 20% unwanted leakage. The anticancer potential MIL-100(Fe)/FA cells showed the improvement of selective index (SI) from 3.21 to 12.48 which means that folic acid acts as an effective ligand. The study of cells treated with fluorescence microscopy and flow cytometry analysis reveals the dependence of the receptor on the nanoparticle through endocytosis. Considering the effects of nanoparticles on healthy cells, MIL-100(Fe) and MIL-100(Fe)/FA nanoparticles can be introduced as targeted drug delivery systems for smart targeting breast cancer cells with minimal side effects.

1. Introduction

Cancer is considered the second serious issue of health in human beings with a global incidence of 17 million new cases in 2018 and an estimation of 27.5 million new cases per year by 2040. Despite different strategies such as surgery, radiation, hormone, and immunomodulation therapy, chemotherapy plays a critical role in overcoming the treatment complexity of cancer [1]. Conventional cancer chemotherapy involves the nonspecific distribution of cancer therapeutic agents in the human body which limits the therapeutic dose within cancer cells, while providing excessive toxicity to normal cells, tissues, and organs [2, 3].

Breast cancer has been classified as first-ranked worrying disease among women around the world [4]. According to statistics, more than one million new cases are annually diagnosed with the disease [5, 6]. In the Iranian population, over 502000 women are affected seriously by breast cancer every year [7, 8]. Long treatment duration and cancer surgery issues, chemotherapy, and radiotherapy cause many

problems in patients' normal life [9]. Various efforts have been made toward the development of drug vehicles for controllable drug release that attains minimal side effects and enhanced therapeutic efficacy [10].

Dual armed therapy and real-time monitored treatment trends of tumors called "theranostics" have gained attention in modern cancer treatment [11–13]. Moreover, using smart molecules for targeting, so-called "active targeting," in a nanoscale package harbors both selective tissue internalization and enhanced permeability and retention (EPR) effects of "passive targeting" which mainly accumulates the drug in tumor areas [14, 15].

Tumor-associated antigens (TAA) are defined as "self" antigens that are expressed more abundantly in cancer tissues. TAA gives an advantage to cancer cell progression through a mechanism called "self-tolerance" that leads to immune system escape [16]. Folate receptor α (FOLR1) that is classified as TAA is normally expressed in the normal placenta, fallopian tube, epithelial kidney, lung, breast, and choroid plexus. Remarkably, its overexpression has been noticed in a large number of tumors including nonmucinous ovary and uterus adenocarcinoma, ependymal brain tumors, pleural mesothelioma, testicular choriocarcinoma, nonfunctioning pituitary adenoma, and also, in triple-negative breast, colon, and renal carcinoma progression due to the requirement of folic acid for DNA synthesis [17–21].

Recently, nanomedicine has emerged as the medical application of nanotechnology. Since nanoparticles are very small in size, nanodrug delivery can allow the delivery of drugs with poor solubility in water. For over a decade, nanoparticle-based therapeutics have been studied as tumor-specific therapeutics and diagnostic agents. The targeted nanoparticles can also be designed as either pH-sensitive or temperature-sensitive carriers. The pH-sensitive drug delivery system can deliver and release drugs within the more acidic microenvironment of cancer cells and/or components within cancer cells [22].

During the last few decades, many different types of nanocarriers have been developed for this purpose, such as inorganic mesoporous silica, quantum dots, metal nanoparticles (NPs), organic micelles, liposomes, and dendrimers. However, all nanocarriers have their limitations in biological applications. Liposomes, micelles, and dendrimers usually suffer from low loading capacities, and inorganic porous materials have undesirable toxicity and unacceptable degradability [23]. The nanoporous metal organic frameworks (MOFs) are an emerging class of hybrid crystalline materials built of metal ions/clusters bridged by organic linkers to form one-, two-, or three-dimensional structures [24]. What makes MOF materials outstanding is their exceptionally large surface areas and centers for trapping target analysts, excessively high porosity, and tunability, which were attributed to the absence of dead volume in the structure [25–27]. They have high mechanical, thermal, and chemical stabilities and are used in a wide range of applications, including gas storage [28], membrane separation [29], heterogeneous catalyst [30–32], analytic sensing [33, 34], encapsulation [35], drug delivery [10, 34, 36], and electronics [37, 38]. Prodigiosin (PG) is known as a natural source, autofluorescence, an algicidal, an insecticidal, antiprotozoal, antibacterial, antifungal, antimalarial, and selective anticancer secondary metabolite from *Serratia marcescens* [39].

Herein, the dual function MOF, pH-sensitive MIL-100(Fe), and MIL-100(Fe)/FA have been successfully synthesized for the first time using the electrochemical method. Shielding free prodigiosin with these MOFs results in site-specific targeting of folic acid-positive breast tumors coupled with fluorescence image tracking and chemotherapy.

2. Experimental

2.1. Materials and Methods

2.1.1. Chemicals. 1-Methyl imidazole, 1-chlorododecane, folic acid, bovine serum albumin (BSA), [3-4,5-dimethylthiazol-2-yl]-2, 5-diphenyltetrazolium bromide (MTT), ethanol, methanol, and DMSO were purchased from Merck Company (Darmstadt, Germany). Trimesic acid (H_3BTC) was purchased from Riedel-de Haen. Phosphate-buffered saline pellets (PBS) were purchased from Sigma-Aldrich (St. Louis, MO, USA). Dulbecco's modified Eagle's medium (DMEM) high-glucose, fetal heat-inactivated bovine serum (FBS), trypsin (0.25%), and penicillin/streptomycin were purchased from Gibco® (Gaithersburg, USA). 4, 6-Diamidino-2-phenylindole (DAPI) was purchased from Invitrogen (California, USA). MCF-7 and skin fibroblast were obtained from the Pasteur Institute of Iran. All other chemicals were analytically graded without any purification. Prodigiosin was purified and prepared according to previously described methods [40].

2.1.2. Apparatus. The synthesized MIL-100(Fe) and MIL-100(Fe)/FA crystalline structures were characterized using Bruker D8 advance X-ray diffraction (XRD) at a 3°/min scanning rate with copper radiation (Cu K, $\lambda = 0.15418$ nm emission, 40 kV/40 mA). The morphology and structure of synthesized MIL-100 were characterized by scanning electron microscopy (SEM) at an accelerating voltage of 30 kV and DSR nanostructure coater and transmission electron microscopy (TEM) using LEO906E microscope. The Fourier transform infrared (FTIR) spectra were obtained using a SHIMADZU-8300 infrared spectrophotometer (Shimadzu, Tokyo). The hydrodynamic size and net surface charge are evaluated using Horiba SZ-100 (Horiba, Japan). MOF texture properties including average surface area, pore volume, and pore size were investigated with N_2 adsorption/desorption by BET technique (BELSORP MINI II). Before measuring pore properties, samples were activated by degassing under vacuum at 150°C for 3 h to remove all water molecules. Drug loading content, release kinetics, and viability assay was investigated through absorption behavior of PG and MTT reagents using UV-Vis absorption spectrophotometer (Shimadzu, Japan) and plate reader (Tecan infinite-200 M Pro, Tecan Co, Switzerland), respectively. Cellular morphology and behavior were monitored using a fluorescence microscope (Olympus; IX51, Olympus Inc., USA).

2.2. Synthesis

2.2.1. Synthesis of 1-Dodecyl, 3-Methyl Imidazolium Chloride [C_{12}mimCl] as Ionic Liquid (IL). The IL was synthesized by mixing 8 mL of 1-methylimidazole and 23.5 mL 1-chlorododecane, and then, the mixture was refluxed without additional solvent at 65°C with constant stirring for 72 h. The product was then dissolved in 8 mL diethyl ether for purifying by washing six times before drying overnight at 70°C under a vacuum [41].

2.2.2. Electrochemical Synthesis of MIL-100(Fe). The electrochemical synthesis of MIL-100(Fe) was done according to the following procedure. Initially, two different solutions containing H_3BTC (0.68 g of H_3BTC to 20 mL ethanol (solution A)) and [C_{12}mimCl] (0.72 g of [C_{12}mimCl] to 10 mL ethanol (solution B)) were prepared separately and stirred for at least 30 min. After reaching completely clear solutions, both solutions were mixed up under stirring conditions at 40°C. Then, two iron plates at a distance of 1 cm were located into the cell containing solution and a voltage of about 30 V (current, 0.9 A) was applied under argon gas for 90 min at 40°C. After completing the reaction, the product was separated from the solution by centrifugation at 6000 rpm for 10 min. The final product (brown precipitate) was rinsed twice with water and ethanol and finally dried in the oven at 80°C for 12 h.

2.2.3. Electrochemical Synthesis of MIL-100(Fe)/FA. For the synthesis of MIL-100(Fe)/FA nanostructures, solutions A and B (according to Section 2.2.2) and solution C (containing 0.02 gr folic acid in 15 mL ethanol) were prepared. After the addition of solution, A to B, solution C was added dropwise to the mixture. After proper stirring, two iron plates (at a distance of 1 cm) were immersed into the mixture, and a voltage of about 30 V (current, 0.9 A) was applied between them for 90 min at room temperature. Argon gas was purged into the reaction mixture during the synthesis. The synthesized MIL-100(Fe)/FA precipitate was centrifuged and kept in ethanol for 24 h, then washed out three times with an excess amount of ethanol to remove the remaining precursor within cavities. Finally, the purified MIL-100(Fe)/FA was dried at room temperature.

More importantly, folic acid was conjugated to the surface of MIL-100(Fe) for targeted drug delivery. Consequently, the MOF-based drug vehicle showed pH-dependent progressive release behavior and good anticancer efficacy. The schematic presentation of the above synthesis methods is shown in Figure 1.

2.3. Drug Loading and Release Procedure

2.3.1. Drug Loading. To calculate the drug loading yield, prodigiosin concentration was initially determined using its molar extinction coefficient, $\varepsilon_{\lambda 535} = 112000\ \mathrm{M^{-1}\,cm^{-1}}$, in ethanol: HCl solution (24 : 1) [40]. Drug loading capacity is crucial for the formulation of drug delivery systems because it directly affects the therapeutic dose available for the targeted tissue. For the calculation of drug loading capacity, a solution of 3 mL of PBS (pH~7.4) containing 1 mg of each MOF was dispersed using an ultrasound sonicate for 10 minutes. Then, the 3.21×10^{-2} μmole of purified PG was added to a phosphate-buffered saline (PBS) solution containing MOFs. This procedure was repeated until the drug adsorption capacity of MOFs reached the saturation state which was represented by the pink color of the supernatant [42]. The loading capacity was calculated by the following equation:

$$\text{Loading capacity}\,(\%) = \frac{\text{wieght of loaded drug on nano particle}}{\text{weight of nanoparticles}} \times 100. \tag{1}$$

To calculate the loading efficiency, the precipitate was collected by centrifugation at the speed of $2000 \times g$ for at least 5 minutes, followed by measuring its maximum absorbance values at $\lambda = 35$ nm before and after the addition of carriers. The loading efficiency was calculated using the following equation [43]:

$$\text{Loadng efficiency}\,(\%) = \frac{\text{drug initial weight} - \text{drug weight in supernatant solution}}{\text{initial drug initialweight}}. \tag{2}$$

2.3.2. Drug Release. The release profiles of PG were investigated in acidic (pH~5.5 and 6.5) and neutral conditions (pH ~7.4). Briefly, 1 mg of both drug-loaded MOFs containing 30 μg PG was dispersed in 5 mL of physiological buffer, PBS, at pH~7.4, pH~6.5, and pH~5.5 for 5 minutes. In the second step, bovine serum albumin (BSA) was added to the solution to reach the final concentration of 1 mg·mL^{-1}. After appropriate time intervals (0 min, 15 min, 30 min, 60 min, 2 h, 3 h, 4 h, and 24 h), 500 μL of supernatant was collected, centrifuged at 6000 rpm for 5 min, and mixed with an equal volume of acidified methanol. To retain a given vial, an equal volume of fresh media was replaced at each sample point. The PG release profile release-10(Fe)@PG and MIL-100(Fe)/FA@PG were calculated using the following equation [43]:

$$\text{Drug releas}(\%) = \frac{C_T - C_0}{C_L} \times 100. \tag{3}$$

In this equation, C_T (mg·mL^{-1}) is defined as the weight of the drug released into the solution from the MIL-100(Fe)@PG or MIL-100(Fe)/FA@PG at a given time, C_0 (mg·mL^{-1}) is the weight of the drug in the supernatant at the initial time (0 minutes), and C_L (mg·mL^{-1}) is the total amount of loaded drug in the MIL-100(Fe)/FA or MIL-100(Fe)/FA@PG nanocomposites.

2.4. Antineoplastic Assessment. The antineoplastic assessment of MIL-100(Fe)@PG or MIL-100(Fe)/FA@PG was determined against human breast cancer cell line, MCF-7, and normal human skin fibroblast cells. Cells were initially cultured in high-glucose Dulbecco's Modified Eagle's Medium (DMEM) supplemented with 10% heat-

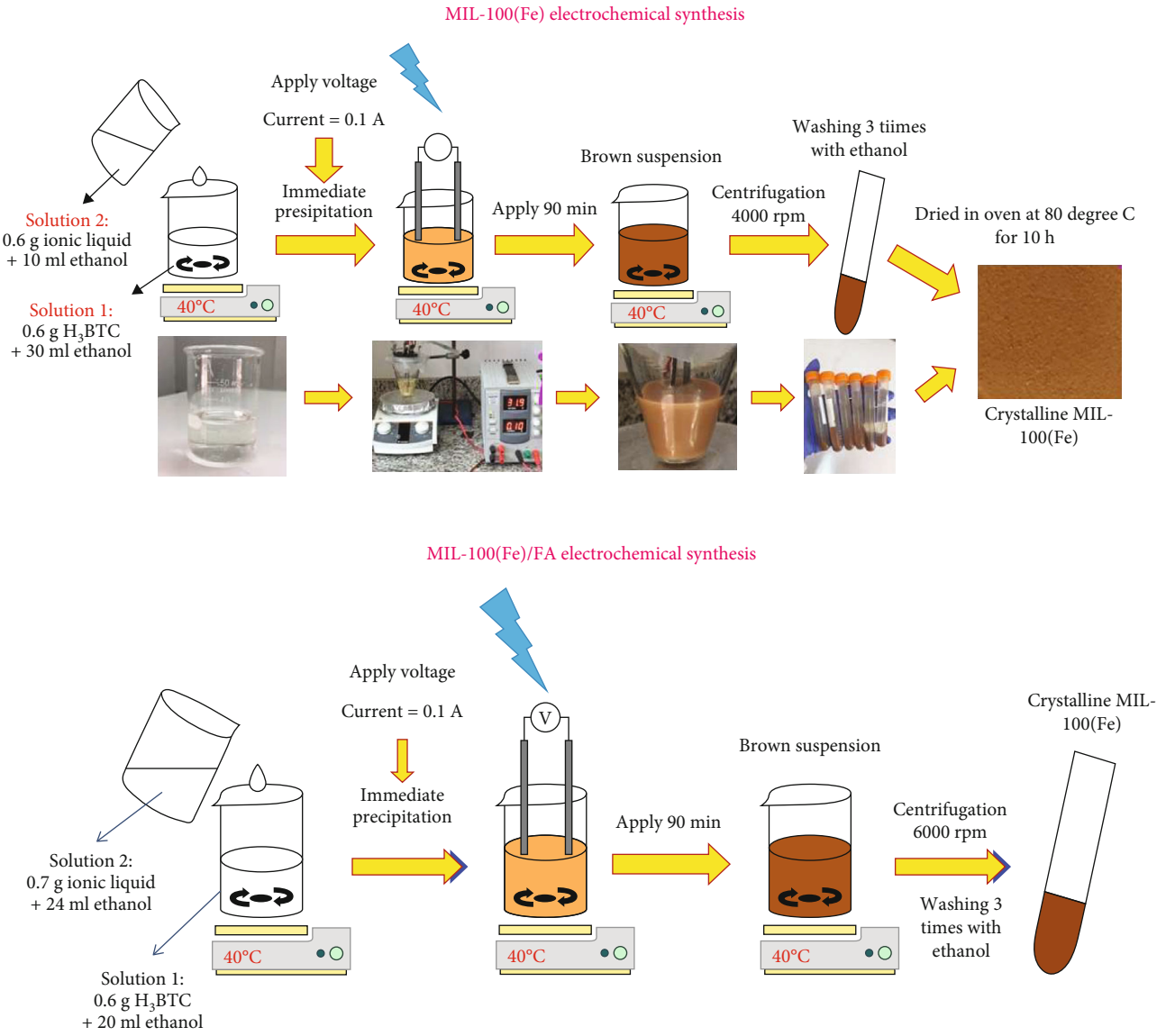

Figure 1: Schematic illustration of the MOF synthesis procedures.

inactivated fetal bovine serum (FBS) and 1% penicillin/streptomycin at 37.0°C under a humidified atmosphere containing 5% CO_2.

Before performing antitumor tests, the basal cell toxicity of blank nanostructures on the cell lines was investigated using elevated concentrations ranging from 50 to 700 $\mu g{\cdot}mL^{-1}$ of MOF nanostructures for 24 and 48 hours. In this propose, 3 mg of MIL-100(Fe) and MIL-100(Fe)/FA were dissolved in 1 mL of PBS, pH~7.4, and dispersed with ultrasound sonication for 3 minutes. After growing the cells to the confluence of 70%, MCF-7 and skin fibroblast cells were detached with 0.25% trypsin, resuspended in DMEM, and seeded in 96-well plates at a concentration of 1×10^4 and 1.5×10^4 cells/well overnight, respectively. The next day, the medium was replaced by increasing concentrations of free PG (0.187, 0.375, 0.750, 1.500, 3.000, and 6.000 $g{\cdot}mL^{-1}$), MIL-100(Fe)@PG, and MIL-100(Fe)/FA@PG (50.0, 100.0, 200.0, 400.0, 500.0, 600.0, and 700.0 $\mu g{\cdot}mL^{-1}$) that is calculated to be equivalent to the free concentration of PG. After appropriate times of incubation (4, 8, 12, and 24 h), cells were washed twice with PBS and incubated in a fresh medium containing 10 μL of MTT solution (5.0 $mg{\cdot}mL^{-1}$). After incubation for 4 h at 37.0°C, the culture medium was removed, and the formazan crystals were dissolved in solubilizing buffer (40% DMF, 16% SDS, pH adjusted to pH~4.7 with acetic acid). The formazan absorbance was measured at 570 nm using a Tecan infinite-200 M Pro microplate reader. The cell viability was determined as follows [44]:

$$\text{Viability}(\%) = \frac{\text{Abs.sample} - \text{Abs.blank}}{\text{Abs.negative control} - \text{Abs.blank}} \times 100. \quad (4)$$

2.5. Fluorescence Microscopy. To investigate the cellular uptake efficiency of MIL-100(Fe) @ PG or MIL-100(Fe)/FA @ PG fluorescence microscopy was done. Initially, 2×10^5 MCF-7 and normal human skin fibroblast cells were precultured in a 24-well plate for 16 hours. Then, a new medium containing $2\,\mu g{\cdot}mL^{-1}$ of free PG and an equal concentration of PG loaded on $100\,\mu g{\cdot}mL^{-1}$ of MOFs was replaced followed by incubating at certain time points (30 min, 12, 16, and 24 h) at the above-mentioned condition. After the time required, cells were washed 3 times with PBS and fixed with 3.7% formaldehyde solution for 10 min. Then, washing was repeated 3 times with PBS and replaced with 0.2% Triton X-100 medium. Finally, cells were stained with 300 nM DAPI for 5 min and examined with a fluorescence microscope (Olympus; IX51, Olympus Inc., USA) under the magnifications of 200x, and the Cell Sense acquisition software was used for image analysis.

2.6. Flow Cytometry Analysis. Flow cytometry analysis was done on both cancerous and normal fibroblast cells. To this end, 5×10^5 MCF-7 and skin fibroblast cells were seeded in 6-well plates overnight. Then, the culture medium was replaced with a fresh medium containing 20 and $2\,\mu g{\cdot}mL^{-1}$ of drug-loaded MOFs and free PG and incubated for an additional 24 h inappropriate conditions, respectively. The adherent cells were collected from the plate through trypsin treatment followed by centrifugation at 700 g for 5 min to remove the supernatant, washed with PBS, and resuspended in FACS buffer containing $0.5\,mg{\cdot}mL^{-1}$ BSA. Finally, fluorescence histograms were determined with the FACSCALIBUR BD flow cytometer (Becton & Dickinson and Co., USA) using a 488 nm argon-ion excitation laser. The gate was arbitrarily set for the detection of red fluorescence (613 nm band-pass filters related to PE/Texas Red) to analyze 10000 gate events per histogram.

2.7. Statistical Analysis. The zetapotential and release percentage of the synthesized nanostructures were presented as average ± SD ($n = 3$). The analysis of the dose-response curve was done using GraphPad Prism software, (version 7.2 San Diego, CA, USA). The results from three independent cell viability experiments were averaged and statistically analyzed using Student's t-test with the significance threshold at the level of $P < 0.05$.

3. Results and Discussions

For over a decade, nanoparticle-based theranostics have been studied as two armed tumor-specific therapeutics and diagnostic agents. Dual fluorescent tracking/targeted delivery systems can achieve real-time monitoring of tumor localization and the therapeutic effect to provide suitable drug delivery guidance. Intravenous chemotherapy, as a standard route of neoplastic drug delivery, is facing serious challenges maintaining the balance between destroying cancerous cells and adverse effects on normal ones. On the other hand, using cell tracker techniques like magnetic resonance spectroscopy (MRS), magnetic resonance imaging (MRI), optical fluorescence and bioluminescence, targeted ultrasound, single-photon emission computed tomography (SPECT), and positron emission tomography (PET) enables scientists to monitor cancer cell associations noninvasively [45, 46]. To this end, loading of red fluorescence active PG to obtain PG @MIL-100(Fe) and PG@MIL-100(Fe)/FA NPs was done. The system provides both pH-responsive drug release and fluorescence monitoring capability for theranostic approaches to *in vitro* dual-modal folic acid positive cancer cell imaging and therapy.

Among different selecting strategies, targeting tumor cells through TAA is used as a valuable means of smart cancer therapy [43, 47]. Folate receptors made of folic acid are frequently overexpressed by cancer cells, conjugated between MIL-100(Fe). In this work, MIL-100(Fe) and MIL-100(Fe)/FA were successfully synthesized by the electrochemical method. To the best of our knowledge, this is the first report on the electrochemical synthesis of these moieties. This research provided a method to produce porous and crystalline MIL-100(Fe) and MIL-100(Fe)/FA from iron plates and trimesic acid in ethanolic solution at ambient conditions. In this method, a metallic plate of the desired metal source of MOF is used. The metallic plate is placed in an electrochemical cell as an electrode. The electrochemical cell is filled with a supporting electrolyte containing a solution of the organic linker of MOF. Upon applying an appropriate voltage or current, the metal plate (anode) is dissolved, and the metal ions required for the MOF formation are released near the electrode surface. The metal ions then immediately react with the linkers present in the solution, and the MOF structure is formed close to the electrode surface. The main advantage of this method is the possibility to control the oxidation state of the metal by simply applying either the appropriate voltage (amperometry mode) or current (potentiometry mode) to the electrode [48]. Also, the physicochemical properties, cytotoxicity, and targeted delivery of newly synthesized MIL-100(Fe) were investigated.

There are many ways to synthesize MOFs, such as hydrothermal, microwave-assisted, and solvothermal synthesis methods. As another efficient synthesis method that has been improved recently, electrochemical synthesis was chosen for this study because of providing the possibility of pure synthesis due to a pure metallic source used in this method. Iron, zinc, calcium, magnesium, and manganese can be considered as suitable metal nodes for synthesizing MOFs which may be used as drug carriers. Iron, however, has shown the capacity to form a safe and nontoxic cluster. Several MOFs have displayed stability in biological fluids for extended periods, such as MIL-100(Fe) which shows potential for healthcare applications [25, 49, 50]. MIL-100(Fe) is one of the highest porous MOFs. The hierarchically mesoporous crystalline three-dimensional iron (III) trimesate has two sets of mesoporous cages (24 Å and 29 Å) that are accessible through microporous windows (ca. 8.6 Å and ca. 4.7-5.5 Å).

3.1. Structural Characterization of MIL-100(Fe) and MIL-100(Fe)/FA. The newly synthesized MIL-100 (Fe) is

characterized using XRD, SEM, TEM, FTIR, DLS, zetapotential, and BET analysis. As illustrated in Figure S1a, the diffraction patterns of XRD indicate that the samples were well-crystallized, and the peak positions were consistent with previously reported MIL-100(Fe) samples. The MIL-100(Fe) shows diffraction peaks at 3.4°, 3.9°, 4.9°, 5.3°, and 11°, corresponding to the (022), (113), (004), (333), and (428) planes of MIL-100, respectively [51]. As mentioned previously, "the coordination of diamond-like shapes MIL-100(Fe) particles produces small pore opening in each cell unit" [52].

The presence of functional groups on the synthesized MIL-100(Fe) and MIL-100(Fe)/FA surface were identified by FTIR spectra (Figure S1b). The vibrational bands at around 1443, 1383, 757, and 708 cm^{-1} are typical of the MIL-100(Fe) framework [53]. Two peaks at 1446 and 1373 cm^{-1} indicate the presence of O–H bending in the plane. The amine peaks are usually weak, and the amount of O–H in this structure shields the peak of the amine group. The presence of amine groups could be further confirmed by the bending vibrations that belong to NH scissoring in the 1620 and 1563 cm^{-1}. Two stretching peaks (1042 and 1085 cm^{-1}) could also be assigned to C–N bonds. The main difference between MIL-100(Fe) and MIL-100(Fe)/FA relies on 1070 to 1530 cm^{-1}, where the peak of FA is separated into several peaks. In the FTIR spectra of FA, the wideband 3650 to 3300 cm^{-1} is due to O-H stretching vibrations, and a characteristic peak that appears at 1684 cm^{-1} is assigned to the stretching vibrations of the C=O of carboxyl groups. FTIR spectra confirm the successful incorporation of the folic acid conjugated to MIL-100(Fe), and the folate groups were successfully grafted onto the amine groups of MOFs which showed good agreement with similar reports [54].

Developing new nanocarriers for oncological treatments to enhance the EPR (enhanced permeability and retention) effect which allows extravasation leakage of particles up to~400 nm to the tumor environment without distribution to healthy tissues helped scientists to develop successful passive targeting systems [55] (see Figure 2). On the other hand, nanoparticles with a diameter between 10 to 200 nm have a longer circulation half-life due to the renal and complement system escape [56]. Moreover, it has been suggested that for spherical nanoparticles, the maximum size limit should be kept to 150 nm to avoid filtration in the spleen [57]. To this end, the size and morphology of MIL-100(Fe) and MIL-100(Fe)/FA nanostructures were investigated with the help of SEM and TEM images. According to Figure 3, the synthesized MIL-100(Fe) and MIL-100(Fe)/FA nanoparticles have a spherical structure with crystals of about 50-200 nm which is a relatively proper size for using as a nanocarrier for longer half-life in the bloodstream. According to TEM images, MIL100(Fe) showed the crystalline phase in polyhedron shape that FA incorporation did not alter the crystal structure. After the addition of FA to the structure, the size of MIL-100(Fe) increased from 103.7 ± 5.9 to 126.1 ± 4.2 nm. The hydrodynamic size of MIL-100(Fe) and MIL-100(Fe)/FA nanoparticles was also showed a slight increase from 125.1 ± 32.9 to 136.3 ± 40.0 nm, respectively. After PG encapsulation, both of MIL-100(Fe)@PG and MIL-100(Fe)/FA@PG showed the size increase up to 152.7 ± 20.4 and 173 ± 24.3 nm, respectively. Simply, the newly synthesized MIL-100(Fe) is large enough to accumulate in the bloodstream, escape from the immune system and liver/spleen filtration, penetrate through leaky tumor vessels, and sustain in the tumor microenvironment for a longer time due to the dysfunctional lymphatic system. Moreover, the functionalization of MIL-100(Fe) with folic acid as TAA led to its extensive uptake by tumor cells rather than normal ones which also satisfied the active targeting purpose.

Zeta potential was used to investigate the electrical potential and surface charge of MOFs in the physiological environment. The MIL-100(Fe) net charge is reduced from +15.1 to +10.9 after the addition of folic acid to the MOF structure, which is probably due to the presence of negatively charged folic acid. As reported earlier, neutral or slightly positive hydrophilic nanoparticles enjoy easier immune system escape, lower unwanted protein adsorption, and enhanced cellular uptake [58, 59]. Protein adsorption on the surface of the nanoparticle promotes opsonization, leading to aggregation and subsequently rapid clearance from the bloodstream through mononuclear system phagocytosis in the liver and the spleen [39].

To investigate the porous structure of the synthesized MOF sample, Brunauer-Emmet-Teller (BET) analysis was carried out. Figure S2 a, b, and Table S1 showed the N2 adsorption/desorption isotherm of the dehydrated MIL-100(Fe) and MIL-100(Fe)/FA. The BET areas of MIL-100(Fe) and MIL-100(Fe)/FA are about 1350 and 831.84 m^2/g, respectively. Also, the EDS spectrum represented the corporation of Fe ions in MIL-100(Fe) structure (Figure S2c and Table S2). These values are close to the reported values for MOFs [11]. The total pore volume of MIL-100(Fe) and MIL-100(Fe)/FA are estimated to be 0.32 and 0.13 cm^3/g, and the pore size distribution of MIL-100(Fe) and MIL-100(Fe)/FA are observed at 24.20 and 20.06 Å.

3.2. Analytical Studies of Drug Loading and Release. Drug loading content is one of the key factors in drug delivery system formulation due to its effects on the therapeutic dose available within the targeted tissue [22]. The prodigiosin loading process was performed using stepwise adsorption of diluted prodigiosin in PBS solution at the final concentration of 10 μM. This process was continued until both MIL-100 (Fe) and MIL-100 (Fe)/FA reached the saturation loading capacity of 38.04 and 36.64% with the help of a standard calibration curve (see Figure S3), respectively. Then, the loading efficiency of MIL-100(Fe) and MIL-100(Fe)/FA was calculated to be 97.07 and 93.43%, respectively.

The targeted nanoparticles can also be designed as pH, enzyme, or temperature-sensitive carriers. The pH-sensitive drug delivery system can deliver and release drugs within the more acidic microenvironment of cancer cells and/or components within cancer cells [22]. Nanoparticles harboring tumor-specific antigens (TAA) are mainly uptake through clathrin-mediated endocytosis [12]. After cellular internalization, MIL-100(Fe) and MIL-100(Fe)/FA

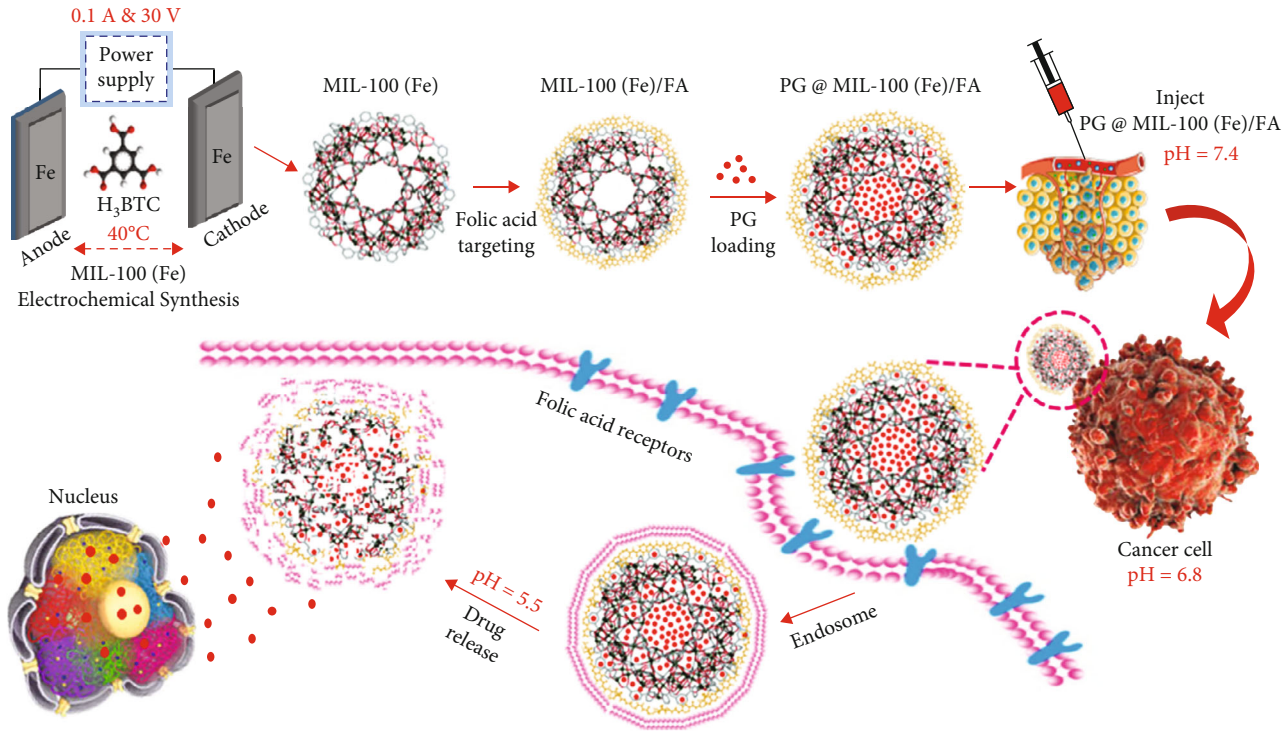

Figure 2: Schematic procedure of PG@MIL-100(Fe)/FA-targeted delivery.

nanoparticles (that were surrounded by double-layer vesicles) are mixed with primary endosomes to generate secondary endosomes for endosome/lysosome digestion. In the secondary endosomes, vacuolar-type proton adenosine triphosphatase (v-ATPase) pumps produce an acidic environment between pH values of 4.7 and 5.5 [13, 60, 61]. In this step, PG is released due to the pH-responsive swelling effect of the MIL-100(Fe) network followed by its endosomal escape to the cytoplasm and eventually reaching the final cargo, the nucleus, to sustain its cell toxicity. After reaching the desired pH, more than 60 hydrolyzing enzymes (like carbohydrate hydrolases, nucleases, proteases, phosphatases, lipases, and others) are activated and hydrolyze the secondary endosomal content to their simple monomeric building blocks [61].

In the glycolysis pathway in the cytoplasm of the normal cells, glucose converts to pyruvate, and thereafter, pyruvate is transferred to the oxygen-consuming mitochondria to produce ATP and carbon dioxide as byproducts. Tumor cells always faced anaerobic conditions, which cause lactic acid production from pyruvate in the cytosol that is called the "Warburg effect" even in the presence of low content of oxygen. Due to the presence of large amounts of lactic acid and the overexpression of Na^+/H^+ exchanger (NHE), HCO^{3-} transporter, vacuolar-ATPase, and the H^+/K^+ ATPase, the pH value of tumor extracellular matrix (tumor microenvironment) decreases from 7.4 to 6.8 [62–64]. In human MCF-7 cells, the microenvironment pH has been measured to be as low as pH 6.44 [64]. *In vitro* drug release profile of MIL-100(Fe)@PG and MIL-100(Fe)/FA@PG were monitored in three different pH values including neutral (pH 7.4) and acidic (pH 6.5, and 5.5) conditions that represented the pH values of the bloodstream, cancer cell microenvironment, and secondary endosomes, respectively [13, 65]. The kinetic release profiles of prodigiosin from the MIL-100 (Fe) and MIL-100(Fe)/FA nanostructure were evaluated in Figure 4. According to the data, the diffusion of prodigiosin from MIL-100(Fe)/FA was faster in acidic and slower in basic medium. The PG percentages of 69.25% and 73.06% were released after 24 hours in an acidic environment while unwanted leakage reached 21.58 and 16.24% in MIL-100(Fe)@PG and MIL-100(Fe)/FA@PG, respectively. This trend indicated a slower release of folic acid-functionalized MIL-100(Fe) compared to MIL 100 (Fe). Also, after 48 hours of incubation, the percentage of soluble drug in buffer decreased due to the PG natural hydrophobicity which led to its tendency to return to the MOF cavities (data not sown). Other FA functionalized MOF structures like 5-FU@UiO-67-(NH)2-FAM/PMT nanoparticles have shown faster release (100% relative release) after 16 hours postincubation at pH 6.4 and 5.0 [34].

3.3. Toxicity Assessment. Before examining the anticancer properties of PG-loaded MOFs, it is necessary to evaluate the toxicity of the MOFs themselves. To investigate the undesirable side effects of the MIL-100(Fe) network, the basal cell toxicity of MIL-100(Fe) was investigated against primary (normal skin fibroblast) cells using a concentration ranging from 50 to 600 $\mu g \cdot mL^{-1}$. Fibroblast cells are one of the most sensitive cells to xenobiotic materials like drugs.

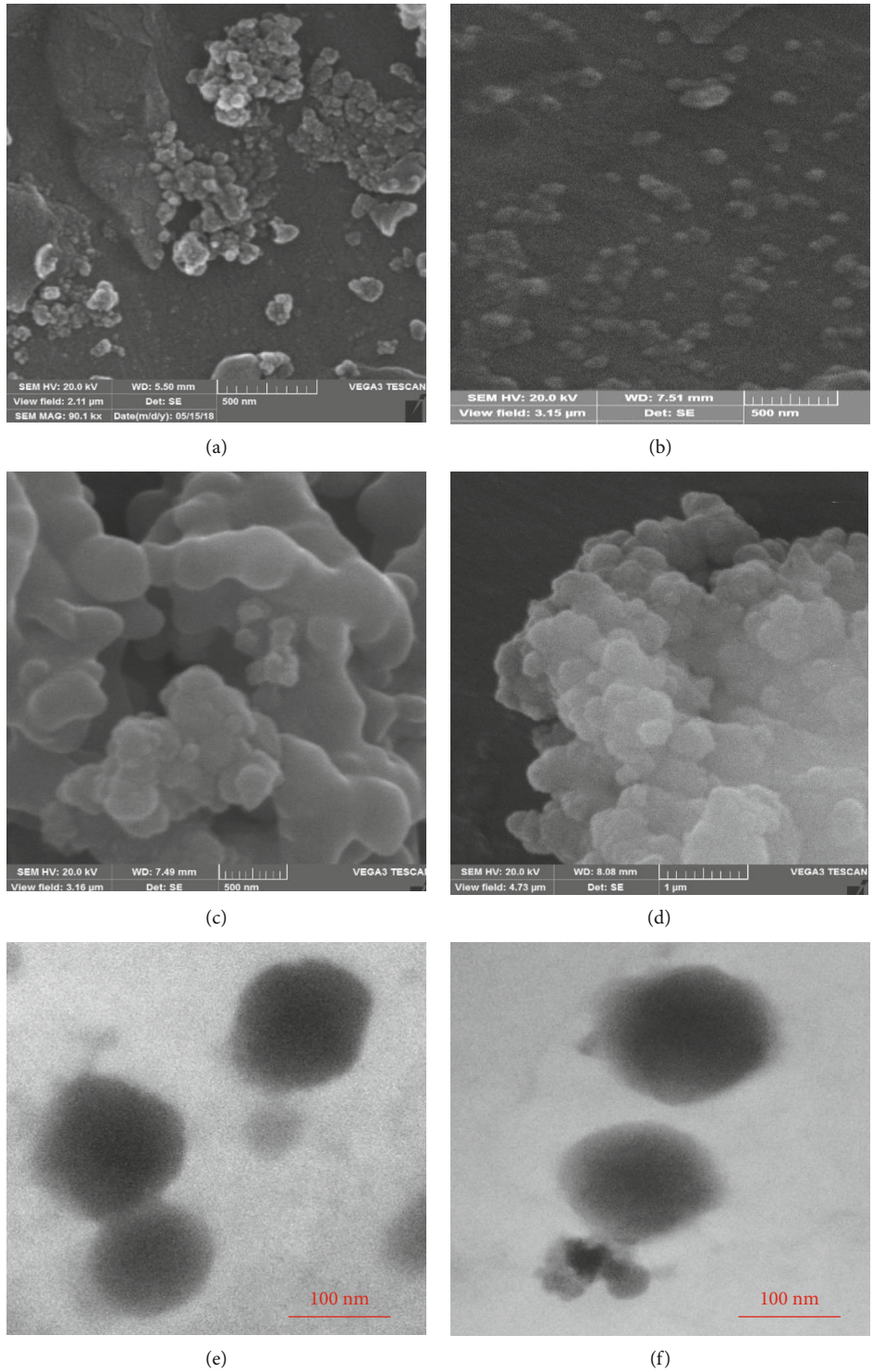

Figure 3: The SEM images of (a) MIL-100 (Fe), (b) MIL-100 (Fe)/FA, (c) MIL-100 (Fe)@PG, and (d) MIL-100 (Fe)/FA@PG. The TEM images of (e) MIL-100 (Fe) and (f) MIL-100 (Fe)/FA.

Herein, we investigated the basal cell toxicity of our delivery system to gain the toxicity threshold. As shown in Figure S4a and S4b, although MIL-100(Fe) nanoparticles have cell toxicity at concentrations over 400 and 300 $\mu g \cdot mL^{-1}$ on the cancerous cell line, MCF-7, no significant difference was observed between the negative control and the cells exposed to increasing concentrations MIL-100(Fe) @PG and MIL-100(Fe)/FA@PG up to this concentration. As illustrated in Figures S4c and S4d, the nanoparticles were toxic at concentrations above 100 $\mu g \cdot mL^{-1}$, indicating higher sensitivity of normal cells compared with cancerous ones, and the addition of folic acid did not show any

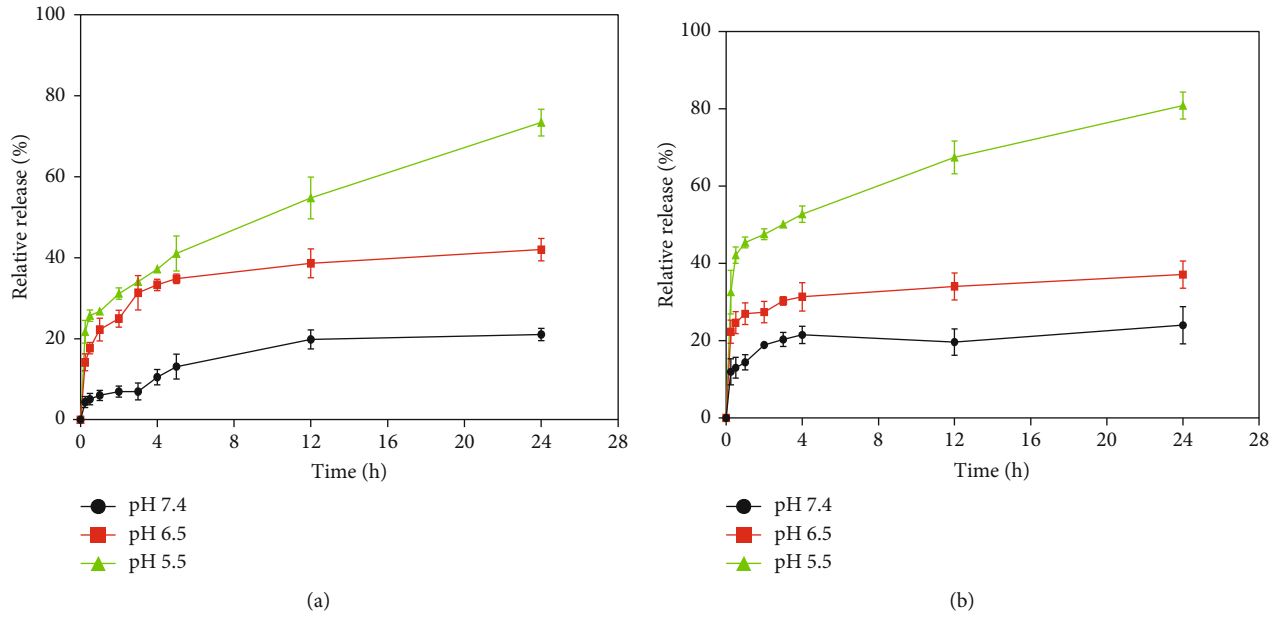

FIGURE 4: In vitro releasing profile of PG-loaded (a) MIL-100(Fe)@PG and (b) MIL-100(Fe)/FA@PG in PBS solution containing 1 mg·mL^{-1} BSA at pH = 7.4, 6.5, and 5.5 and 37°C. Kinetic release data are presented as the average ± SD ($n = 3$) in three independent experiments.

significant difference on normal fibroblast cells. Therefore, both MIL-100 (Fe) frameworks are suitable to be used as a carrier within the threshold of 200 μg·mL^{-1} and 100 μg·mL^{-1} of nanocarriers on cancerous and normal tissue targets, respectively. The fitting curve of all treatments is also shown in Figure S5.

After evaluating the toxicity of the nanoparticles alone, nanoparticles loaded with PG were used on MCF-7 and skin fibroblasts and the percentage of viability was estimated through monitoring mitochondrial NADH-dependent dehydrogenase activity. To this end, different concentrations of free PG and MIL-100(Fe)@PG and MIL-100(Fe)/FA@PG were tested within three different time points (8, 24, and 48 h) on MCF-7 and skin fibroblast cells which presented as inhibitory concentration (IC_{50}) values. To calculate the antitumorigenic ability of MIL-100(Fe)@PG 1.15-18.5 μM of PG loaded on to 6.25-100 μg·mL^{-1} of MOF and folic acid-functionalized MIL-100(Fe) carriers was compared with free administration of PG. According to Figure S4c and S4d graphs, the vital effects of PG loaded are time-dependent in both cancer and normal cell lines. Based on these results, IC_{50} obtained from 8, 24, and 48 h incubation of free pG on MCF-7 cells were calculated to be 3.37 ± 1.58, 2.62 ± 0.49 , and 2.0 ± 41.20, respectively. This trend is also detected on skin fibroblast cells with higher IC_{50} values of 11 ± 0.58, 7.62 ± 0.65, and 7.0 ± 74.55 μM as compared with cancer cell lines, respectively. This difference is mostly related to the well-known selectivity anticancer of PG that has been reported elsewhere [66, 67]. The IC_{50} values of first 8 hours for MIL-100(Fe(@PG and MIL-100(Fe)/FA@PG treatment on MCF-7 cell line were calculated to be 11.41 ± 1.01 and 3.92 ± 1.6 μM compared to skin fibroblasts that were 14.99 ± 1.14 and 16.58 ± 1.10 , respectively. After 24 hours of incubation, the IC_{50} of PG-loaded MIL-100(Fe)@PGandMIL-100(Fe)/FA@PG on MCF-7 cell line was equal to 4.71 ± 1.32 and 3.03 ± 0.21 μM, while skin fibroblast cells showed IC_{50} values around 15.00 ± 1.14 and 17.5 ± 0.21 μM, respectively. Finally, IC_{50} obtained after 48 hours of incubation on MIL-100(Fe)@PG and MIL-100(Fe)/FA@PG on MCF-7 cell line were 4.02 ± 0.21 and 1.10 ± 0.32 Mm compared with 16.44 ± 1.32 and 17.00 ± 0.30 μM on skin fibroblast cells, respectively. Moreover, due to the different IC_{50} values of selective anticancer drugs, the selective index (SI) value of the free drug was also represented the relative successfulness of drug targeting approaches (see Figures 5(a) and 5(b)). For this purpose, the selected index (IC_{50} value on cancer cell/IC_{50} value on healthy cell) of the free drug was calculated to be 3.21, while in MIL-100 (Fe)@PG it reached 4.08 and in MIL-100(Fe)/FA@PG it increased by 12.87. This trend indicates that folic acid-functionalized MIL-100(Fe) was able to improve the targeting ability up to 3.15-fold greater than MIL-100(Fe)@PG. These results indicated that the MIL-100 (Fe)/FA possessed an apparent ability to target folic acid-overexpressed cells and could efficiently release PG into the cargo, elevating anticancer efficacy and reducing side effects. Also, MIL-100(Fe)/FA is capable of being used as a carrier for hydrophobic compounds like PG to its cargo with slow-release kinetics and, hence, minimum side effects on normal cells.

3.4. Intracellular Uptake Study. Up to now, autofluorescent anticancer drugs, like doxorubicin, daunorubicin, and curcumin, have been used for noninvasive real-time fluorescent monitoring not only *in vitro* but also *in vivo* as tumor trackers [68, 69]. The specific cellular accumulation of

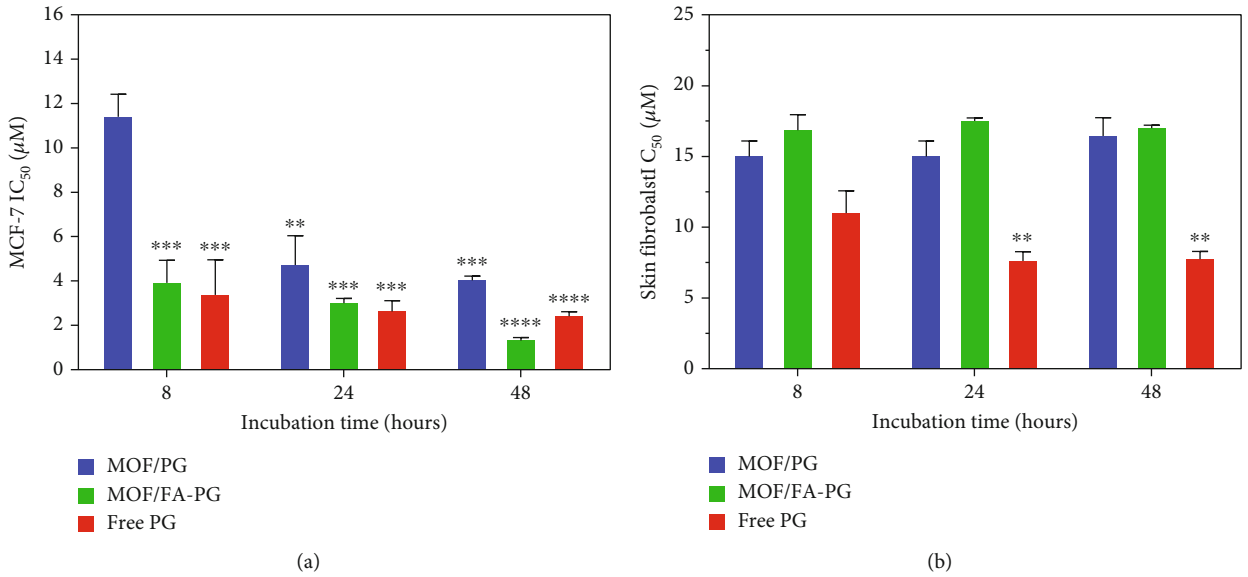

Figure 5: The selective index (SI) values of MIL-100(Fe)@PG and MIL-100 (Fe)/FA@PG were compared with free PG against (a) MCF-7 and (b) normal skin fibroblast cells after 8, 24, and 48 h exposure. Free prodigiosin was kept at an equal concentration with drug-loaded MOFs. All mentioned data are displayed as the average ± SD ($n = 3$). The statistical evaluation of IC50 was compared pairwise between IC50 of each treating time and maximum concentration of the drug used as a control (IC50 = 30.75 μM for normal fibroblast and IC50 = 6 μM for MCF-7 was considered as untreated cells), using t-test with $^{*}(P$ value $\leq 0.05)$, $^{**}(P$ value $\leq 0.01)$, $^{***}(P$ value $\leq 0.001)$, $^{****}(P$ value $\leq 0.0001)$ significance values.

natural fluorescence pigment prodigiosin was done to investigate the real-time monitoring of the cellular uptake kinetics of designed MOF nanocarrier, using both fluorescence microscopy and flow cytometry.

3.4.1. Fluorescence Microscopy. As illustrated in Figure 6, the cytoplasmic accumulation of free PG was fast enough that was noticed within the first 30 minutes on both cancerous and normal cell populations and uniformly observed up to 24 hours posttreatment. This trend is mostly related to the hydrophobic properties of PG to pass the cellular membrane [66]. The cellular toxicity of free administration of PG on cells also showed that there had been significant cellular morphology changes on normal fibroblast cells after 16 hours of incubation.

As mentioned in Figures S6a and b, cellular uptake of MIL-100(Fe) nanocarriers by MCF-7 cells was time-dependent, starting slowly from 30 min incubation and raised to maximum concentration after 24 h with small morphological changes. Compared with cellular accumulations of PG on MCF-7 cells, the MIL-100(Fe) entry into the skin fibroblast cells was lower even after 24 hours of incubation, although rounded cellular morphology was also observed after 16 hours of incubation. Similar to MIL-100(Fe)@PG cellular uptake, MIL-100(Fe)/FA@PG treatment showed the time-dependent cellular uptake by MCF-7 cells (see Figure S7a). As shown in Figure S7b, cellular accumulation was not detectable until 16 hours of incubation in skin fibroblasts without significant morphological changes, indicating low side effects of MIL-100(Fe)/FA@PG. However, it was significantly observed after 12 h postincubation in the cancer cells, indicating a higher diffusion of PG in MCF-7 than in the normal cells.

3.4.2. Flow Cytometry Analysis. To investigate the cellular uptake enhancement of PG-loaded nanocarriers in total populations, drug entry of loaded nanoparticles in two MCF-7 cell lines and skin fibroblasts were analyzed using flow cytometry analysis over 8 hours. The greater PG concentration shift was observed in cancerous cells, while lower fluorescence intensity in normal cells would suggest improved drug incorporation into the target cells with minimal side effects on normal ones. The fluorescence intensity shifts within the cellular population would also reflect the successful cellular uptake of PG-loaded MOFs compared with free PG. As shown in Figure 7(a), the fluorescence emission of the whole cell population dramatically shifted in samples treated with free PG, which indicated the successful entrance of the drug into the cells. The treatment of MCF-7 cells with MIL-100(Fe)/FA@PG particles loaded with PG also showed similar and close release rates to the free PG state in most cell populations. The mean fluorescence intensity indicated that PG entry into MCF-7 cells was about 94.7% due to the presence of folate receptors on the surface of MIL-100 (Fe)@PG. This process was observed to a lesser extent in the cellular population treated with MIL-100(Fe)@PG particles, which indicated that approximately 77.9% of the cells had small content of PG-containing MOFs in MCF-7 cells. To take a brief look at normal fibroblast cell populations harboring free and PG-loaded MOFs (see Figure 7(b)), there has been a significant PG entrance blockage in both MIL-100 (Fe) and MIL-100 (Fe)/FA@PG samples which clearly shows the reduced side effects on normal cells compared to free the administration of PG.

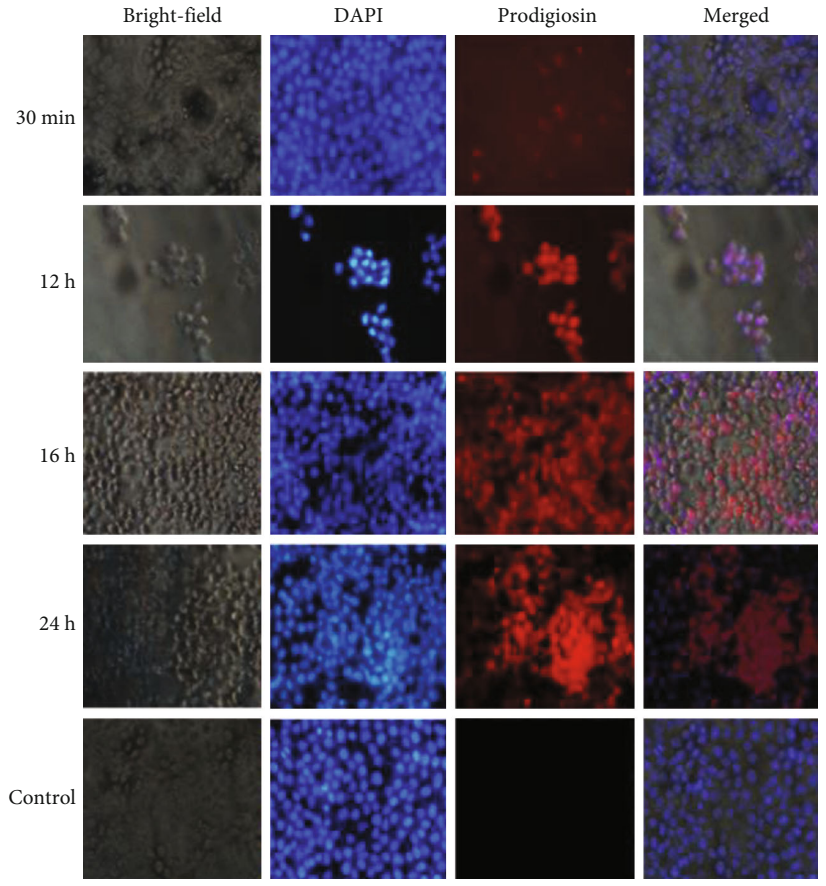

(a)

Figure 6: Continued.

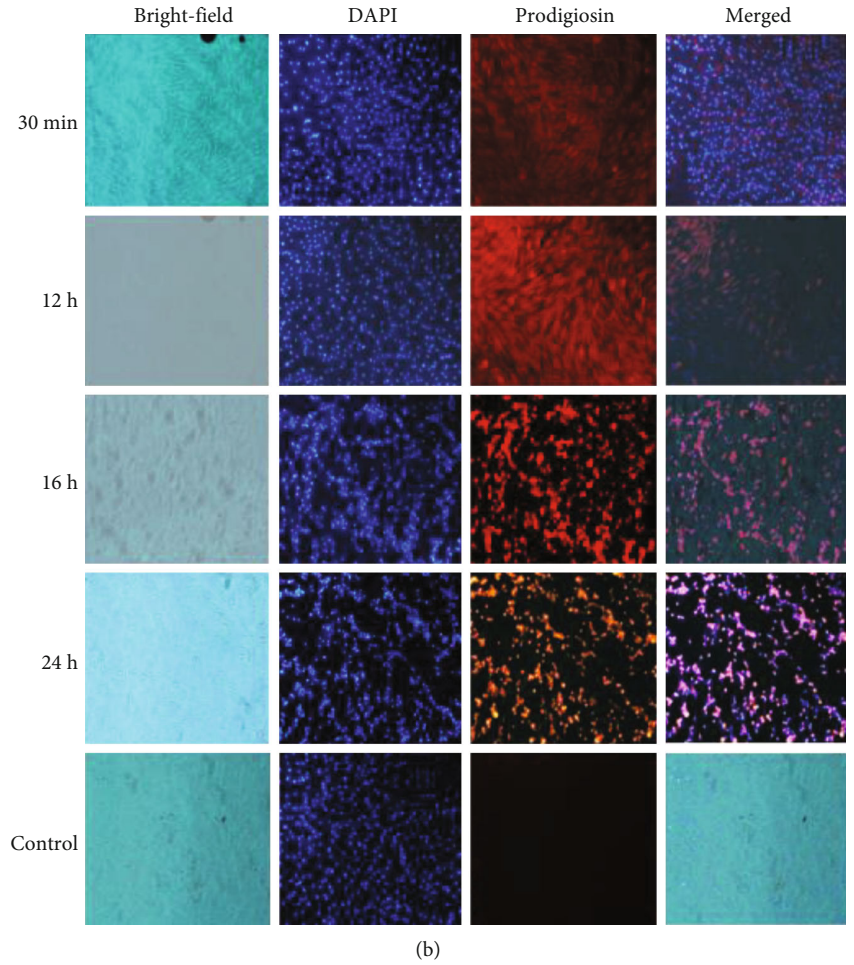

Figure 6: The cellular uptake of free PG on (a) MCF-7 and (b) skin fibroblast cell lines after 30 minutes, 12, 16, and 24 hours of incubation compared with untreated cell lines as control. Bright field shows the cellular morphology, while DAPI, PG, and merged represent the nucleus, PG, and cellular localization of PG on treated cells, respectively.

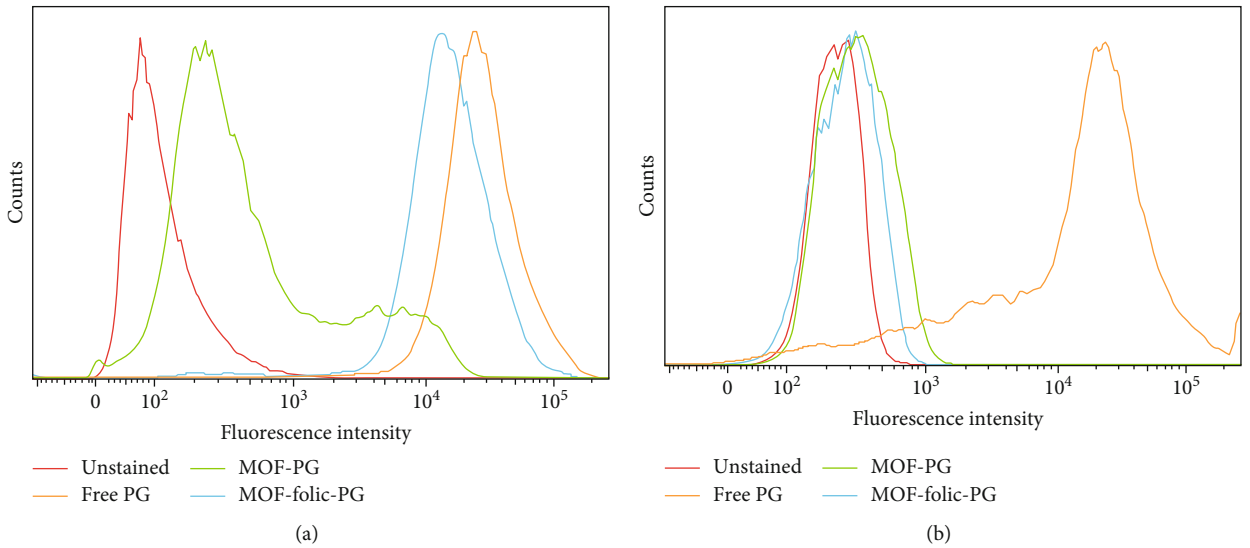

Figure 7: The cellular uptake content of cell populations treated with the free PG, PG-loaded MIL-100(Fe), and MIL-100(Fe)/FA on (a) MCF-7 and (b) normal skin fibroblast after 8 hours of incubation compared with untreated control cells. The free PG and PBS solutions were introduced as positive and negative controls, respectively.

4. Conclusion

In conclusion, we investigated pH stimuli-responsive drug delivery systems with low toxicity, easy to functionalized, biodegradable, and high therapeutic efficacy to deliver hydrophobic therapeutic compounds like prodigiosin. Most importantly, additional investigations like *in vivo* research should be done to clear their long-term toxicity with these systems which are conducted to determine possible side effects before their clinical trials.

Abbreviations

A: Absorbance
BET: Brunauer, Emmett, and Teller
BSA: Bovine serum albumin
BTC: 1,3,5-Benzene tricarboxylic acid
BUS: Busulfan
DAPI: 4′,6-Diamidino-2-phenylindole
DDS: Drug delivery system
DMF: Dimethylformamide
DMSO: Dimethyl sulfoxide
DNA: Deoxyribonucleic acid
DL: Drug loading
DLC: Drug loading capacity
DLE: Drug loading efficiency
DR: Drug release
EDX: Energy dispersive X-ray spectroscopy
EPR: Enhanced permeability and retention
FA: Folic acid
FTIR: Fourier transform infrared spectroscopy
HF: Hydrochloric acid
HSA: Human serum albumin
IC50: Inhibitory concentration
IL: Ionic liquid
IUPAC: International Union of Pure and Applied Chemistry
MCF-7: Michigan Cancer Foundation-7
MCM-41: Mobil Composition of Matter No. 41
MIL: Material of Institute lavalier
MOF: Metal organic framework
MTBS: Methyltributyl ammonium methyl sulfate
MTT: 3-(4,5-dimethylthiazol-2-yl)-2diphenyltetrazolium bromide
PBS: Phosphate-buffered saline
PG: Prodigiosin
PS: Phosphatidyl serine
ROS: Reactive oxygen specious
RPM: Revolutions per minute
T: Transmittance
TAA: Tumor-associated antigens
TC: Tetracycline
XRD: X-ray diffraction
ZIF: Zeolitic imidazolate framework.

Data Availability

Data are available within the article.

Conflicts of Interest

The authors declare that they have no conflicts of interest.

Acknowledgments

We acknowledge the Nanotechnology Research Institute of Shiraz University, Central Laboratory of Shiraz University of Medical Sciences, and the Ministry of Science and Technology as providers of financial support and contributions.

Supplementary Materials

Figure S1: the (a) XRD patterns and (b) FTIR spectra of MIL-100(Fe) and MIL-100(Fe)/FA. Figure S2: BET analysis of N2 adsorption/desorption in (a) MIL-100(Fe) and (b) MIL-100(Fe)/FA. (c) EDS spectra of MIL-100(Fe). Figure S3: the calibration curve of PG in (a) methanol: PBS buffer (1 : 1) and (b) absolute methanol. Figure S4: in vitro toxicity analysis of MIL-100 (Fe), free PG, and PG-loaded MIL-100 (Fe), and MIL-100 (Fe)/FA nanocarriers. Biocompatibility of (a, c) MIL-100 (Fe) and (b, d) MIL-100 (Fe)/FA was investigated after 24 and 48 h on MCF-7 and normal skin fibroblast cells, respectively. The PG-loaded MIL-100 (Fe) and MIL-100 (Fe)/FA cellular toxicity were compared with free PG against (c) MCF-7/GFP and (d) normal skin fibroblast cells were determined with the help of the inhibitory concentration (IC50) after 8, 24, and 48 h exposure. Free prodigiosin was kept at an equal concentration with drug-loaded MOFs. All mentioned data are displayed as the average ± SD ($n = 3$). The statistical evaluation of IC50 was compared pairwise between IC50 of each treating time and maximum concentration of the drug used as a control (IC50 = 30.75 μM for normal fibroblast and IC50 = 6 μM for MCF-7 was considered as untreated cells), using t-test with $^{*}(P$ value $\leq 0.05)$, $^{**}(P$ value $\leq 0.01)$, $^{***}(P$ value $\leq 0.001)$, and $^{****}(P$ value $\leq 0.0001)$ significance values. Figure S5: the fitting curve diagram treatment of free PG on (a) MCF-7 and (b) normal skin fibroblast cells, treatment of PG-loaded MIL-100(Fe) on (c) MCF-7 and (d) normal skin fibroblast cells and PG-loaded MIL-100(Fe)/FA on, (e) MCF-7 and (f) normal skin fibroblast cells after 8, 24, and 48 h of exposure. All mentioned data are displayed as the average ± SD ($n = 3$). Figure S6: the cellular uptake of PG-loaded MIL-100(Fe) on (a) MCF-7 and (b) skin fibroblast cell lines after 30 minutes, 12, 16, and 24 hours of incubation compared with untreated cell lines as control. Bright field shows the cellular morphology, while DAPI, PG, and merged represent the nucleus, PG, and cellular localization of PG on treated cells, respectively. Figure S7: the cellular uptake of PG-loaded MIL-100(Fe)/FA on (a) MCF-7 and (b) skin fibroblast cell lines after 30 minutes, 12, 16, and 24 hours of incubation compared with untreated cell lines as control. Bright field shows the cellular morphology, while DAPI, PG, and merged represent the nucleus, PG, and cellular localization of PG on treated cells, respectively. Table S1: BET analysis information for synthesized MIL-100(Fe) and MIL-100(Fe)/FA. Table S2: the weight percentage of various elements using EDS analysis. *(Supplementary Materials)*

References

[1] V. T. DeVita and E. Chu, "A history of cancer chemotherapy," *Cancer Research*, vol. 68, no. 21, pp. 8643–8653, 2008.

[2] Q. Wu, Z. Yang, Y. Nie, Y. Shi, and D. Fan, "Multi-drug resistance in cancer chemotherapeutics: mechanisms and lab approaches," *Cancer Letters*, vol. 347, no. 2, pp. 159–166, 2014.

[3] E. Pérez-Herrero and A. Fernández-Medarde, "Advanced targeted therapies in cancer: drug nanocarriers, the future of chemotherapy," *European Journal of Pharmaceutics and Biopharmaceutics*, vol. 93, pp. 52–79, 2015.

[4] E. Taeidi, S. Montazeri, N. Behroozi, M. H. Haghighy Zadeh, and A. Ahmadzadeh Deilami, "The effect of problem solving therapy on breast cancer women," *International Journal of Cancer Management*, vol. 11, 2018.

[5] C. E. DeSantis, J. Ma, A. Goding Sauer, L. A. Newman, and A. Jemal, "Breast cancer statistics, 2017, racial disparity in mortality by state," *CA: a Cancer Journal for Clinicians*, vol. 67, no. 6, pp. 439–448, 2017.

[6] M. K. Mejdahl, K. G. Andersen, R. Gartner, N. Kroman, and H. Kehlet, "Persistent pain and sensory disturbances after treatment for breast cancer: six year nationwide follow-up study," *BMJ*, vol. 346, no. apr11 1, article f1865, 2013.

[7] D. Cronin-Fenton, M. Nørgaard, J. Jacobsen et al., "Comorbidity and survival of Danish breast cancer patients from 1995 to 2005," *British Journal of Cancer*, vol. 96, no. 9, pp. 1462–1468, 2007.

[8] S. M. Mousavi, M. M. Gouya, R. Ramazani, M. Davanlou, N. Hajsadeghi, and Z. Seddighi, "Cancer incidence and mortality in Iran," *Annals of Oncology*, vol. 20, no. 3, pp. 556–563, 2009.

[9] A. Joy, M. Ghosh, R. Fernandes, and M. J. Clemons, "Systemic treatment approaches in her2-negative advanced breast cancer—guidance on the guidelines," *Current Oncology*, vol. 22, Suppl 1, pp. S29–S42, 2015.

[10] P. Horcajada, T. Chalati, C. Serre et al., "Porous metal-organic-framework nanoscale carriers as a potential platform for drug delivery and imaging," *Nature Materials*, vol. 9, no. 2, pp. 172–178, 2010.

[11] S. E. MORADI, S. DADFARNIA, A. M. HAJI SHABANI, and S. EMAMI, "Microwave-enhanced Fenton-like degradation by surface-modified metal–organic frameworks as a promising method for removal of dye from aqueous samples," *Turkish Journal of Chemistry*, vol. 41, no. 3, pp. 426–439, 2017.

[12] S. Behzadi, V. Serpooshan, W. Tao et al., "Cellular uptake of nanoparticles: journey inside the cell," *Chemical Society Reviews*, vol. 46, no. 14, pp. 4218–4244, 2017.

[13] F. R. Maxfield and D. J. Yamashiro, "Endosome acidification and the pathways of receptor-mediated endocytosis," *Immunobiology of proteins and peptides IV*, pp. 189–198, 1987.

[14] S. P. Dunuweera, R. M. S. I. Rajapakse, R. B. S. D. Rajapakshe, S. H. D. P. Wijekoon, M. G. G. S. Nirodha Thilakarathna, and R. M. G. Rajapakse, "Review on targeted drug delivery carriers used in nanobiomedical applications," *Current Nanoscience*, vol. 15, no. 4, pp. 382–397, 2019.

[15] K. Greish, "Enhanced permeability and retention (EPR) effect for anticancer nanomedicine drug targeting," in *Cancer Nanotechnology*, pp. 25–37, Springer, 2010.

[16] R. Reilly, L. Emens, and E. Jaffee, "Humoral and cellular immune responses: independent forces or collaborators in the fight against cancer?," *Current opinion in investigational drugs*, vol. 2, no. 1, pp. 133–135, 2001.

[17] H. Elnakat and M. Ratnam, "Distribution, functionality and gene regulation of folate receptor isoforms: implications in targeted therapy," *Advanced Drug Delivery Reviews*, vol. 8, no. 56, pp. 1067–1084, 2004.

[18] B. M. Necela, J. A. Crozier, C. A. Andorfer et al., "Folate receptor-α (FOLR1) expression and function in triple negative tumors," *PLoS One*, vol. 10, no. 3, article e0122209, 2015.

[19] L. E. Kelemen, "The role of folate receptor α in cancer development, progression and treatment: cause, consequence or innocent bystander?," *International Journal of Cancer*, vol. 119, no. 2, pp. 243–250, 2006.

[20] G. L. Zwicke, G. Ali Mansoori, and C. J. Jeffery, "Utilizing the folate receptor for active targeting of cancer nanotherapeutics," *Nano reviews*, vol. 3, no. 1, p. 18496, 2012.

[21] J. LArias, "Drug targeting strategies in cancer treatment: an overview," *Mini Reviews in Medicinal Chemistry*, vol. 11, no. 1, pp. 1–17, 2011.

[22] N. Mishra, "Targeted drug delivery: a review," *American Journal of PharmTech Research*, vol. 6, pp. 2249–3387, 2016.

[23] M. X. Wu and Y. W. Yang, "Metal–organic framework (MOF)-based drug/cargo delivery and cancer therapy," *Advanced Materials*, vol. 29, no. 23, p. 1606134, 2017.

[24] M. Meilikhov, K. Yusenko, D. Esken, S. Turner, G. van Tendeloo, and R. A. Fischer, "Metals@ MOFs–loading MOFs with metal nanoparticles for hybrid functions," *European Journal of Inorganic Chemistry*, vol. 2010, no. 24, pp. 3701–3714, 2010.

[25] B. Singco, L. H. Liu, Y. T. Chen, Y. H. Shih, H. Y. Huang, and C. H. Lin, "Approaches to drug delivery: Confinement of aspirin in MIL-100(Fe) and aspirin in the _de novo_ synthesis of metal -organic frameworks," *Microporous and Mesoporous Materials*, vol. 223, pp. 254–260, 2016.

[26] D. Yuan, "Porous materials to store clear energy gases," *Advanced Nanomaterials and Their Applications in Renewable Energy*, p. 297, 2015.

[27] J. L. Rowsell and O. M. Yaghi, "Metal–organic frameworks: a new class of porous materials," *Microporous and Mesoporous Materials*, vol. 73, no. 1-2, pp. 3–14, 2004.

[28] M. Eddaoudi, J. Kim, N. Rosi et al., "Systematic design of pore size and functionality in isoreticular MOFs and their application in methane storage," *Science*, vol. 295, no. 5554, pp. 469–472, 2002.

[29] Z. Y. Yeo, S. P. Chai, P. W. Zhu, and A. R. Mohamed, "An overview: synthesis of thin films/membranes of metal organic frameworks and its gas separation performances," *RSC Advances*, vol. 4, no. 97, pp. 54322–54334, 2014.

[30] A. M. Rasero-Almansa, A. Corma, M. Iglesias, and F. Sánchez, "Design of a bifunctional Ir–Zr based metal–organic framework heterogeneous catalyst for the N-alkylation of amines with alcohols," *ChemCatChem*, vol. 6, no. 6, pp. 1794–1800, 2014.

[31] Y. P. Wu, J. W. Tian, S. Liu et al., "Bi-microporous metal–organic frameworks with cubane [M4(OH)4] (M=Ni, Co) clusters and pore-space partition for electrocatalytic methanol oxidation reaction," *Angewandte Chemie*, vol. 131, no. 35, pp. 12313–12317, 2019.

[32] M.-L. Hu, V. Safarifard, E. Doustkhah et al., "Taking organic reactions over metal-organic frameworks as heterogeneous catalysis," *Microporous and Mesoporous Materials*, vol. 256, pp. 111–127, 2018.

[33] M.-L. Hu, S. A. A. Razavi, M. Piroozzadeh, and A. Morsali, "Sensing organic analytes by metal–organic frameworks: a new way of considering the topic," *Inorganic Chemistry Frontiers*, vol. 7, no. 7, pp. 1598–1632, 2020.

[34] W. Liu, Y. Pan, Y. Zhong et al., "A multifunctional aminated UiO-67 metal-organic framework for enhancing antitumor cytotoxicity through bimodal drug delivery," *Chemical Engineering Journal*, vol. 412, article 127899, 2021.

[35] L. Paseta, G. Potier, S. Abbott, and J. Coronas, "Using Hansen solubility parameters to study the encapsulation of caffeine in MOFs," *Organic & Biomolecular Chemistry*, vol. 13, no. 6, pp. 1724–1731, 2015.

[36] W. Liu, Q. Yan, C. Xia et al., "Recent advances in cell membrane coated metal–organic frameworks (MOFs) for tumor therapy," *Journal of Materials Chemistry B*, vol. 9, no. 22, pp. 4459–4474, 2021.

[37] V. Stavila, A. A. Talin, and M. D. Allendorf, "MOF-based electronic and opto-electronic devices," *Chemical Society Reviews*, vol. 43, no. 16, pp. 5994–6010, 2014.

[38] K.-G. Liu, F. Rouhani, H. Moghanni-Bavil-Olyaei et al., "A conductive 1D high-nucleus silver polymer as a brilliant non-hybrid supercapacitor electrode," *Journal of Materials Chemistry A*, vol. 8, no. 26, pp. 12975–12983, 2020.

[39] D. E. Owens III and N. A. Peppas, "Opsonization, biodistribution, and pharmacokinetics of polymeric nanoparticles," *International Journal of Pharmaceutics*, vol. 307, no. 1, pp. 93–102, 2006.

[40] B. Rastegari, H. R. Karbalaei-Heidari, R. Yousefi, S. Zeinali, and M. Nabavizadeh, "Interaction of prodigiosin with HSA and β-Lg: spectroscopic and molecular docking studies," *Bioorganic & Medicinal Chemistry*, vol. 24, no. 7, pp. 1504–1512, 2016.

[41] J. Bowers, C. P. Butts, P. J. Martin, M. C. Vergara-Gutierrez, and R. K. Heenan, "Aggregation behavior of aqueous solutions of ionic liquids," *Langmuir*, vol. 20, no. 6, pp. 2191–2198, 2004.

[42] B. Rastegari, H. R. Karbalaei-Heidari, S. Zeinali, and H. Sheardown, "The enzyme-sensitive release of prodigiosin grafted β-cyclodextrin and chitosan magnetic nanoparticles as an anticancer drug delivery system: synthesis, characterization and cytotoxicity studies," *Colloids and Surfaces B: Biointerfaces*, vol. 158, pp. 589–601, 2017.

[43] S. Kariminia, A. Shamsipur, and M. Shamsipur, "Analytical characteristics and application of novel chitosan coated magnetic nanoparticles as an efficient drug delivery system for ciprofloxacin. Enhanced drug release kinetics by low-frequency ultrasounds," *Journal of Pharmaceutical and Biomedical Analysis*, vol. 129, pp. 450–457, 2016.

[44] T. L. Riss, R. A. Moravec, A. L. Niles et al., *Cell viability assays, in Assay Guidance Manual*, Eli Lilly & Company and the National Center for Advancing Translational Sciences., 2016.

[45] T. F. Massoud and S. S. Gambhir, "Molecular imaging in living subjects: seeing fundamental biological processes in a new light," *Genes & Development*, vol. 17, no. 5, pp. 545–580, 2003.

[46] W. Cai and X. Chen, "Nanoplatforms for targeted molecular imaging in living subjects," *Small*, vol. 3, no. 11, pp. 1840–1854, 2007.

[47] Y. Lu, E. Sega, C. P. Leamon, and P. S. Low, "Folate receptor-targeted immunotherapy of cancer: mechanism and therapeutic potential," *Advanced Drug Delivery Reviews*, vol. 56, no. 8, pp. 1161–1176, 2004.

[48] W.-J. Li, M. Tu, R. Cao, and R. A. Fischer, "Metal–organic framework thin films: electrochemical fabrication techniques and corresponding applications & perspectives," *Journal of Materials Chemistry A*, vol. 4, no. 32, pp. 12356–12369, 2016.

[49] M. S. A. H. Khan, *Solid-state NMR study of nitric oxide adsorption in carboxylate based MOFs*.

[50] P. Horcajada, C. Serre, G. Maurin et al., "Flexible porous metal-organic frameworks for a controlled drug delivery," *Journal of the American Chemical Society*, vol. 130, no. 21, pp. 6774–6780, 2008.

[51] F. Zhang, J. Shi, Y. Jin, Y. Fu, Y. Zhong, and W. Zhu, "Facile synthesis of MIL-100(Fe) under HF-free conditions and its application in the acetalization of aldehydes with diols," *Chemical Engineering Journal*, vol. 259, pp. 183–190, 2015.

[52] M. Nehra, N. Dilbaghi, N. K. Singhal, A. A. Hassan, K. H. Kim, and S. Kumar, "Metal organic frameworks MIL-100(Fe) as an efficient adsorptive material for phosphate management," *Environmental Research*, vol. 169, pp. 229–236, 2019.

[53] R. Liang, R. Chen, F. Jing, N. Qin, and L. Wu, "Multifunctional polyoxometalates encapsulated in MIL-100 (Fe): highly efficient photocatalysts for selective transformation under visible light," *Dalton Transactions*, vol. 44, no. 41, pp. 18227–18236, 2015.

[54] S. D. Taherzade, J. Soleimannejad, and A. Tarlani, "Application of metal-organic framework nano-MIL-100 (Fe) for sustainable release of doxycycline and tetracycline," *Nanomaterials*, vol. 7, no. 8, p. 215, 2017.

[55] L. E. Gerlowski and R. K. Jain, "Microvascular permeability of normal and neoplastic tissues," *Microvascular Research*, vol. 31, no. 3, pp. 288–305, 1986.

[56] S. A. Kulkarni and S.-S. Feng, "Effects of particle size and surface modification on cellular uptake and biodistribution of polymeric nanoparticles for drug delivery," *Pharmaceutical Research*, vol. 30, no. 10, pp. 2512–2522, 2013.

[57] S. M. Moghimi, A. Hunter, and T. Andresen, "Factors controlling nanoparticle pharmacokinetics: an integrated analysis and perspective," *Annual Review of Pharmacology and Toxicology*, vol. 52, pp. 481–503, 2012.

[58] F. Alexis, E. Pridgen, L. K. Molnar, and O. C. Farokhzad, "Factors affecting the clearance and biodistribution of polymeric nanoparticles," *Molecular Pharmaceutics*, vol. 5, no. 4, pp. 505–515, 2008.

[59] M. Wang and M. Thanou, "Targeting nanoparticles to cancer," *Pharmacological Research*, vol. 62, no. 2, pp. 90–99, 2010.

[60] M. Forgac, "Vacuolar ATPases: rotary proton pumps in physiology and pathophysiology," *Nature Reviews Molecular Cell Biology*, vol. 8, no. 11, pp. 917–929, 2007.

[61] S. R. Bonam, F. Wang, and S. Muller, "Lysosomes as a therapeutic target," *Nature Reviews Drug Discovery*, vol. 18, no. 12, pp. 923–948, 2019.

[62] R. J. Gillies, N. Raghunand, M. L. Garcia-Martin, and R. A. Gatenby, "pH imaging," *IEEE Engineering in Medicine and Biology Magazine*, vol. 23, no. 5, pp. 57–64, 2004.

[63] L. Q. Chen and M. D. Pagel, "Evaluating pH in the extracellular tumor microenvironment using CEST MRI and other imaging methods," *Advances in radiology*, vol. 2015, 2015.

[64] R. J. Gillies, N. Raghunand, G. S. Karczmar, and Z. M. Bhujwalla, "MRI of the tumor microenvironment," *Journal of Magnetic Resonance Imaging*, vol. 16, no. 4, pp. 430–450, 2002.

[65] D. Neri and C. T. Supuran, "Interfering with pH regulation in tumours as a therapeutic strategy," *Nature Reviews Drug Discovery*, vol. 10, no. 10, pp. 767–777, 2011.

[66] R. Pérez-Tomás and M. Vinas, "New insights on the antitumoral properties of prodiginines," *Current Medicinal Chemistry*, vol. 17, no. 21, pp. 2222–2231, 2010.

[67] R. Francisco, R. Pérez-Tomás, P. Gimènez-Bonafé, V. Soto-Cerrato, P. Giménez-Xavier, and S. Ambrosio, "Mechanisms of prodigiosin cytotoxicity in human neuroblastoma cell lines," *European Journal of Pharmacology*, vol. 572, no. 2-3, pp. 111–119, 2007.

[68] A. Sahu, N. Kasoju, and U. Bora, "Fluorescence study of the curcumin– casein micelle complexation and its application as a drug nanocarrier to cancer cells," *Biomacromolecules*, vol. 9, no. 10, pp. 2905–2912, 2008.

[69] Y. Kang, W. Sun, J. Fan et al., "Ratiometric real-time monitoring of hydroxyapatite–doxorubicin nanotheranostic agents for on-demand tumor targeted chemotherapy," *Materials Chemistry Frontiers*, vol. 2, no. 10, pp. 1791–1798, 2018.